Atmospheric
Measurement
Techniques

Smithsonian Astrophysical Observatory Ozone Mapping and Profiler Suite (SAO OMPS) formaldehyde retrieval

Gonzalo González Abad[1], Alexander Vasilkov[2], Colin Seftor[2], Xiong Liu[1], and Kelly Chance[1]

[1]Harvard-Smithsonian Center for Astrophysics, Cambridge, MA, USA
[2]NASA Goddard Space Flight Center, Greenbelt, MD, USA

Correspondence to: Gonzalo González Abad (ggonzalezabad@cfa.harvard.edu)

Abstract. This paper presents our new formaldehyde (H_2CO) retrievals, obtained from spectra recorded by the nadir instrument of the Ozone Mapping and Profiler Suite (OMPS) flown on board NASA's Suomi National Polar-orbiting Partnership (SUOMI-NPP) satellite. Our algorithm is similar to the one currently in place for the production of NASA's Ozone Monitoring Instrument (OMI) operational H_2CO product. We are now able to produce a set of long-term data from two different instruments that share a similar concept and a similar retrieval approach. The ongoing overlap period between OMI and OMPS offers a perfect opportunity to study the consistency between both data sets. The different spatial and spectral resolution of the instruments is a source of discrepancy in the retrievals despite the similarity of the physic assumptions of the algorithm. We have concluded that the reduced spectral resolution of OMPS in comparison with OMI is not a significant obstacle in obtaining good-quality retrievals. Indeed, the improved signal-to-noise ratio of OMPS with respect to OMI helps to reduce the noise of the retrievals performed using OMPS spectra. However, the size of OMPS spatial pixels imposes a limitation in the capability to distinguish particular features of H_2CO that are discernible with OMI. With root mean square (RMS) residuals $\sim 5 \times 10^{-4}$ for individual pixels we estimate the detection limit to be about 7.5×10^{15} molecules cm^{-2}. Total vertical column density (VCD) errors for individual pixels range between 40 % for pixels with high concentrations to 100 % or more for pixels with concentrations at or below the detection limit. We compare different OMI products (SAO OMI v3.0.2 and BIRA OMI v14) with our OMPS product using 1 year of data, between September 2012 and September 2013. The seasonality of the retrieved slant columns is captured similarly by all products but there are discrepancies in the values of the VCDs. The mean biases among the two OMI products and our OMPS product are 23 % between OMI SAO and OMPS SAO and 28 % between OMI BIRA and OMPS SAO for eight selected regions.

1 Introduction

H_2CO is ubiquitous in the Earth's troposphere. Background levels in remote regions with concentrations below 1 ppb are due to methane (CH_4) oxidation. Over the continents, hotspots of enhanced concentrations are found due to oxidation of short-lived non-methane volatile organic compounds (NMVOCs) of anthropogenic, biogenic, and pyrogenic origin (secondary sources) or directly emitted by wild fires or industrial activities (primary sources). Concentrations of H_2CO over these hotspots can reach boundary layer levels of 5 ppb or higher (Houweling et al., 1998; Kanakidou et al., 2005; Lowe and Schmidt, 1983; Parrish et al., 2012).

The importance of H_2CO as an atmospheric trace gas resides in its influence in the chemical pathways of tropospheric ozone (O_3) and in the relationship with the concentration of hydroxyl radicals (OH), the main tropospheric oxidant (Anderson et al., 1996). Due to its high reactivity it has a short tropospheric lifetime of a few hours (Brune et al., 1999), making it a useful proxy for NMVOC emissions in satellite observations and for the estimation of top-down emission inventories of isoprene (Barkley et al., 2008; Fu et al., 2007; Marais et al., 2012; Stavrakou et al., 2009a, b, 2014; Zhu et al., 2014). High concentrations of H_2CO can be dangerous to human health, causing eye, nose, and throat

irritation. It is also known to be a human carcinogen. Fortunately, such high concentrations are not found in the open air (Liteplo et al., 2002) since they are consequence of cigarette smoking, pressed-wood products or fuel-burning appliances.

With UV nadir instruments we can sample concentrations in the troposphere, where most of the atmospheric H_2CO is located. The first global H_2CO measurements using UV radiation were reported by Chance et al. (2000), using Global Ozone Monitoring Experiment (GOME) spectra. Since this seminal work, measurements of tropospheric H_2CO have been obtained using data recorded by the SCanning Imaging Absorption spectrometer for Atmospheric CHartography (SCIAMACHY), GOME-2 instruments and Ozone Monitoring Instrument (OMI) (De Smedt et al., 2008, 2012, 2015; González Abad et al., 2015; Hewson et al., 2015; Kurosu et al., 2004; Palmer et al., 2001; Vrekoussis et al., 2010; Wittrock et al., 2006), and now Smithsonian Astrophysical Observatory Ozone Mapping and Profiler Suite (SAO OMPS; this work and Li et al., 2015). Having overlapping retrievals from OMI and OMPS opens the possibility of building a long-term data set of H_2CO using similar retrieval algorithms and having a period of cross-calibration to allow us to extract valuable conclusions about the performance of both instruments that will be of great value for future low-Earth orbit (LEO) and geostationary missions such as the Tropospheric Emissions: Monitoring of Pollution (TEMPO; Chance et al., 2013).

Section 2 includes the description of the SAO OMPS H_2CO retrievals. We describe the characteristics of the instrument, the spectral fitting, the calculation of vertical column densities (VCDs) by using air mass factors (AMFs), and the reference sector normalization of the VCDs. Section 3 presents the error analysis for the VCDs. Section 4 describes the comparison between NASA and Belgian Institute for Space Aeronomy (BIRA) OMI retrievals and the OMPS SAO product. The conclusions are in Sect. 5.

2   SAO OMPS H₂CO observations

2.1   The OMPS Nadir Mapper (OMPS-NM instrument

The OMPS-NM is one of three sensors that compose the OMPS suite of instruments. OMPS-NM was launched on board the Suomi National Polar-orbiting Partnership (Suomi-NPP) satellite on 28 October 2011. Suomi-NPP orbits the Earth at an altitude of 824 km on a polar Sun-synchronous orbit with an inclination of 98.7° (Flynn et al., 2014). Its Equator crossing time in the ascending node is 13:30 local time (LT) which places it close to the afternoon satellites of NASA's A-Train constellation, including Aura. Aura hosts the UV visible spectrometer OMI (Levelt et al., 2006), thus offering a great opportunity for the comparison of the retrievals obtained from both instruments.

The OMPS-NM sensor combines a single grating and a 340×740 pixel charge-coupled device (CCD) array detector. It measures UV radiation covering the spectral range between 300 and 380 nm with a pixel sampling of 0.42 nm and a full width half maximum of 1 nm. It has an instantaneous cross-track field of view of approximately 110°, corresponding to 2800 km at the Earth's surface, providing global daily coverage. For this study we use the OMPS-NM Earth science mode, where measurements are combined in 35 cross-track macropixels given a spatial size of the nadir pixel of 50 km (cross-track) by 50 km (along-track), with an integration period for each measurement of 7.6 s (Dittman et al., 2002; Seftor et al., 2014). The CCD readout is split in the center so that measurements of the central pixel are split, resulting in 36 cross-track pixel positions.

2.2   SAO OMPS H₂CO retrieval

To obtain H_2CO VCDs our algorithm follows a two-step approach. First we perform a direct spectral fit of the measured radiance to obtain slant column densities (SCDs) using the basic optical absorption spectroscopy approach (BOAS; Chance, 1998). The second step converts SCDs to VCDs using look-up tables of precomputed scattering weights to calculate AMFs. The SAO OMPS H_2CO algorithm is similar to the SAO OMI H_2CO retrieval described by González Abad et al. (2015). Modifications are reduced to the minimum required to deal with particular aspects of the OMPS-NM instrument to produce a long-term data set that is as consistent as possible. A more detailed description of the OMI algorithm is in Sect. 2 of González Abad et al. (2015). Here we will briefly describe the characteristics of the OMPS SAO H_2CO retrieval.

2.2.1   Spectral fitting

We have performed a series of studies to select the most suitable fitting window and fitting parameters for OMPS H_2CO. Our main interest was to reduce the correlation between H_2CO columns and the rest of the fitting parameters, especially BrO. We optimized the fitting window at 327.7 to 356.0 nm, different to that used in several consistent GOME, GOME-2, SCIAMACHY, and OMI retrievals, 328.5 to 346.0 nm, which does not include the H_2CO absorption band located around 353 nm (De Smedt et al., 2008, 2012). Figure 1 shows the correlation among H_2CO SCDs and the rest of the fitted gas SCDs for orbit 3538, an overpass of the Americas on 3 July 2012. Even though the correlation between H_2CO and BrO shows two minimal bands between 325 and 326 and 330 and 331 nm, two different considerations prevent the use of them. The first band of low H_2CO-BrO correlations, below 326.5 nm, is discarded due to the increasing strength of O_3 cross sections below 328 nm. The second band is discarded by the increasing correlation between the cross section used to account for the Ring effect
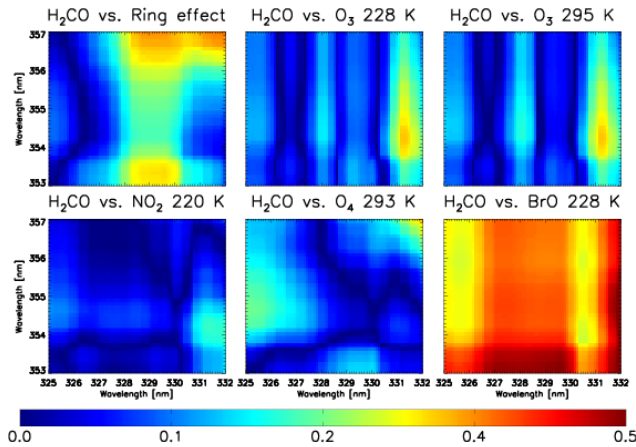
Figure 1. Correlation among H$_2$CO SCDs and other gas SCDs included in the fitting for different fitting windows. The parameter space of the fitting window extremes has been explored in 0.1 nm increments. The value of the x axis indicates the beginning of the fitting window and the y axis the end of it. The correlation values plotted here are the mean values for all the pixels in orbit 3538. Only pixels with solar zenith angles below 70° have been considered.

above 328 nm for fitting windows ending above 356 nm and the increase in the correlations between O$_3$ and H$_2$CO above 330.7 nm.

Another factor we have considered to select the fitting interval is the minimization of fitting uncertainties by increasing the number of spectral points considered. Extending the fitting window above 345 nm allows us to include the H$_2$CO absorption band centered at 353 nm. Including this band also implies including the wing of the O$_2$−O$_2$ band centered at 360 nm. To minimize the correlation between H$_2$CO and O$_2$−O$_2$ we decided to start the fitting window at 327.7 nm, and to include the H$_2$CO absorption band at 353 nm we chose a finishing wavelength of 356 nm.

After selecting the fitting window we perform the direct fit of the measured radiance to the semi-empirical model of the top-of-atmosphere radiance described by Eq. (1). Prior to building the model we wavelength calibrate the radiance by cross-correlating it with a high-resolution solar spectrum (Chance and Kurucz, 2010).

$$I = \left[(aI_0 + \sum_i \alpha_i X_i) e^{-\sum_j \alpha_j X_j} \right] \sum_n \alpha_n X_n + \sum_m \alpha_m X_m \quad (1)$$

The radiance, I, is calculated starting from a mean radiance reference, I_0. We construct I_0 using earthshine radiances over the remote Pacific Ocean, where H$_2$CO concentrations are assumed to be at background levels. These radiances are as close as possible to 165° W and were measured within 1 day of the orbit we are retrieving. With the set of selected radiances over the remote Pacific Ocean we calculate a mean radiance reference for each cross-track position. While computing the mean radiance reference I_0 we

only consider spectra recorded between 30° S and 30° N. The reason behind using the mean radiance reference instead of the solar irradiance spectrum is to avoid cross-track stripes in the retrieval, a common problem in many sensors that use 2-D CCD array detectors (Veihelmann and Kleipool, 2006). The caveat of this solution is that effectively we are retrieving the differential SCDs (ΔSCDs) between the observation and the radiance reference spectra. To account for this fact we apply a correction based on a reference sector normalization, which is described in higher detail in Sect. 2.4 (Khokhar et al., 2005).

In modeling the radiance we also include the effects of the Beer–Lambert law absorption ($e^{-\sum_j \alpha_j X_j}$) with contributions from H$_2$CO (Chance and Orphal, 2011), O$_3$ at two temperatures 228 and 295 K (Malicet et al., 1995), BrO (Wilmouth et al., 1999), NO$_2$ (Vandaele et al., 1998), the O$_2$−O$_2$ collision complex (Thalman and Volkamer, 2013), and the Ring effect (Chance and Spurr, 1997). We also include a correction term to account for instrument undersampling of the spectra ($\sum_i \alpha_i X_i$) (Chance, 1998; Chance et al., 2005). The absorption cross sections are convolved with the OMPS-NM slit functions. The functions were measured prior to launch using a tunable laser to scan the band passes of selected band centers at representative pixel locations on the focal plane; the resulting functions were then iterated to calculate a band-pass for each CCD pixel. The laser was tuned over a wavelength range of ±2 pixels for each of the OMPS-NM sensor band centers. Since the wavelength step size is coarse, approximately 0.4 pixels, five adjacent pixel responses were interpolated to a fine grid and combined to form a single observed band-pass function. In Eq. (1) we are using two closure third-order polynomials ($\sum_n \alpha_n X_n + \sum_m \alpha_m X_m$) to account for low-frequency features of the spectra such as Rayleigh scattering and the effects of aerosols. In Eq. (1), α represents the fitting parameter while X represents the undersampling correction, the cross sections, or the different orders of the polynomials. The characteristics of the spectral fitting are summarized in Table 1. To retrieve the SCDs we use a nonlinear least-squares inversion method implemented in the ELSUNC software (Lindström and Wedin, 1988) to minimize the cost function χ^2 defined as the weighted square difference between the measured and modeled radiance.

Figure 2 shows the result of the fitting for three pixels in orbit 3538 over the Americas. These three pixels have been chosen to illustrate how with just a visual inspection, when the amount of H$_2$CO is big enough, we can clearly distinguish the H$_2$CO signal in the fitting (two top panels with retrieved H$_2$CO concentrations of 1.8×10^{16} and 0.8×10^{16}, respectively), while in the last case, as we approach the detection limit, it is difficult to tell visually whether there is measurable H$_2$CO and we must rely on statistics to obtain the information. Typical retrieved ΔSCDs range between -0.5×10^{15} and 2×10^{16} molecules cm^{-2} for background levels and hotspots with fitting uncertainties of about 4.0×10^{15}.

Table 1. Fitting window and parameters used in the retrieval of H$_2$CO differential slant column densities.

|	
Fitting window	327.7–356.0 nm
Radiance reference spectrum	Computed online over the remote Pacific ocean between 30° N and 30° S
Baseline polynomial	Third order
Scaling polynomial	Third order
Instrument slit function	Pre-flight measurements
Solar reference spectrum	Chance and Kurucz (2010)
H$_2$CO cross sections	Chance and Orphal (2011), 300 K
O$_3$ cross sections	Malicet et al. (1995), 228 K and 295 K
NO$_2$ cross sections	Vandaele et al. (1998), 220 K
BrO cross sections	Wilmouth et al. (1999), 228 K
O$_2$−O$_2$ collision complex cross sections	Thalman and Volkamer (2013), 293 K
Ring effect cross sections	Chance and Spurr (1997)
Undersampling correction	Computed online (Chance et al., 2005)
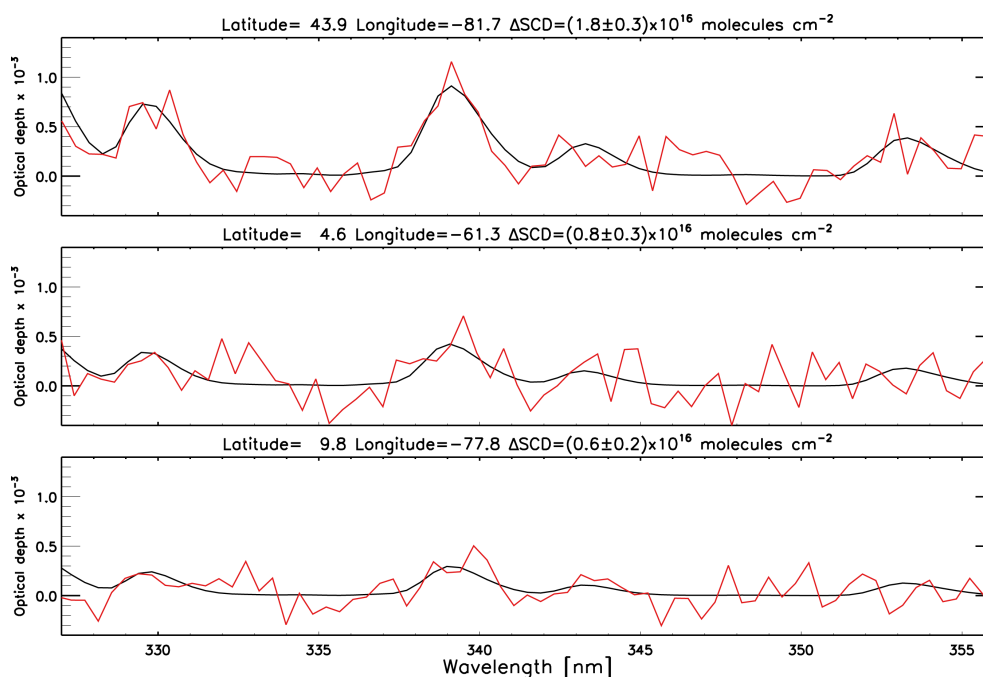
Figure 2. Fitting results of three pixels with decreasing concentrations of H$_2$CO in orbit 3538 outside the SAA. Black lines represent the fitted H$_2$CO optical depth, and red lines the fitted H$_2$CO optical depth plus the fitting residuals.

Figure 3 shows the ΔSCDs, the fitting uncertainty, the solar zenith angle (SZA), and the relative fitting uncertainty for this orbit. The effect of the South Atlantic Anomaly (SAA) in the quality of the retrieval is evident in the ΔSCDs and the fitting uncertainties (swath lines 20–120). Note the increase in the fitting uncertainty as the SZAs increase. Excluding the SAA, the fitting uncertainty remains around 5×10^{15} molecules cm^{-2} or less for SZAs below 70°. To estimate the detection limit we explore the relationship between the root mean square (RMS), H$_2$CO cross sections, and its optical depth using this expression, SCD $\times \sigma_{\mathrm{max}} > $ RMS, where σ_{max} is the maximum H$_2$CO cross section in the fitting window (Schönhardt et al., 2008). With typical RMS values of $\sim 5 \times 10^{-4}$ the detection limit is estimated at $\sim 7.5 \times 10^{15}$ molecules cm^{-2}. As the background concentration due to CH$_4$ oxidation in remote regions is 2 to 7 $\times$ 10^{15} molecules cm^{-2}, the retrieval is unable to clearly resolve background concentrations. This situation is evident when we consider the standard deviation over the remote Pacific Ocean, which is around 4×10^{15} molecules cm^{-2}, similar to the concentrations expected in remote regions.

2.2.2 Slant column to vertical column calculation

The proportionality between VCDs and SCDs can be expressed via AMFs (Eq. 2). The AMFs contain information, some of it a priori, about the state of the atmosphere (gas con-
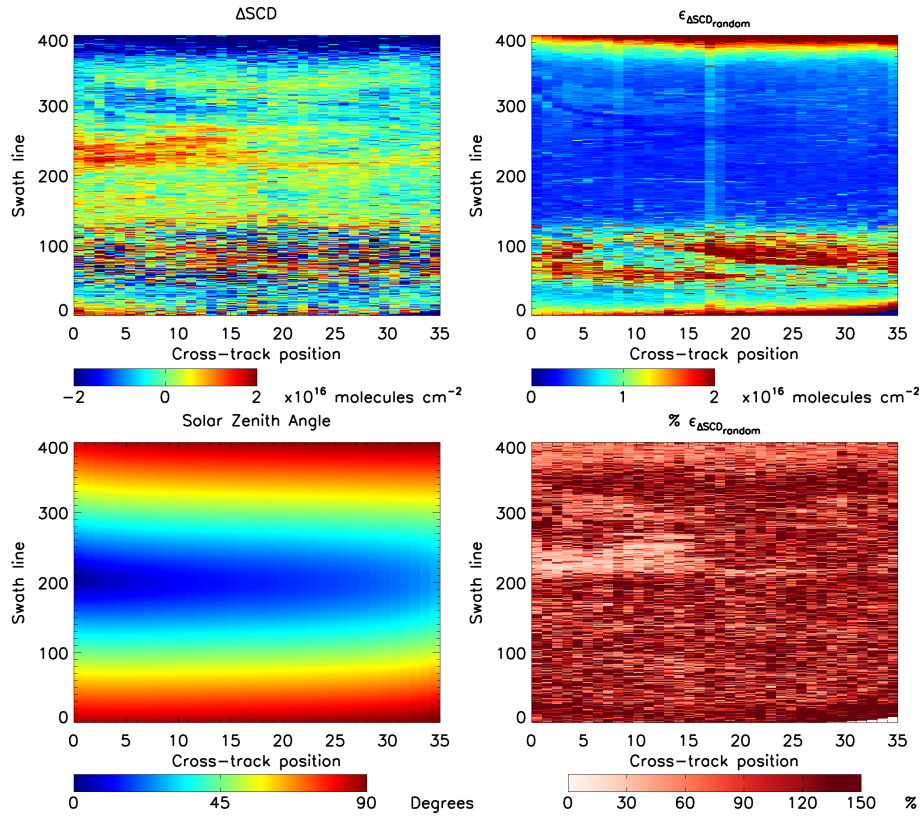
Figure 3. ΔSCD, fitting uncertainty, SZA and relative fitting uncertainty for orbit 3538. The effect of the SAA is clearly visible in the two top panels (swath lines 20 to 120). In the top right panel, which shows the fitting uncertainty, it is possible to appreciate the effect of splitting the central cross-track pixel (Seftor et al., 2014).

centrations, clouds, and aerosols), the characteristics of the spatial pixel footprint (surface reflectance and terrain height), and the geometry of the retrieval.

$$\text{VCD} = \frac{\text{SCD}}{\text{AMF}} \qquad (2)$$

To compute AMFs we follow the theoretical approach described by Palmer et al. (2001). The main idea is that for weak trace gas absorption such as that of H₂CO, we can describe the AMFs as the combination of a shape factor containing information about the vertical distribution of H₂CO concentrations and the scattering weights ($w(z)$) describing how the radiation is transmitted throughout different layers of the atmosphere. $w(z)$ is a function of the geometry of the observation (SZA, viewing zenith angle (VZA), and relative azimuth angle (RAA)), the altitude, the aerosol load, the surface properties (reflectance and altitude), and the characteristics of the clouds present in the scene, if any (cloud fraction and cloud pressure). In our algorithm cloudy pixels are treated by considering the independent pixel approximation (Martin et al., 2002). In this approximation the pixel $w(z)$ is the combination of the cloud-free scattering weight (w_{clear}) and the cloudy scattering weight (w_{cloud}) as shown in Eq. (3) for a given altitude. w_{clear} is a function of the geometry of

the problem, surface albedo (a_{s}), surface elevation (h_{s}), and the altitude while w_{cloud} depends on the cloud albedo (a_{c}), defined here as 0.8, the cloud centroid pressure (c_{p}), and the altitude. Φ is the radiative cloud fraction.

$$w(z) = (1 - \Phi) \cdot w_{\text{clear}}(z, a_{\text{s}}, h_{\text{s}}) + \Phi \cdot w_{\text{cloud}}(z, a_{\text{c}}, c_{\text{p}}) \qquad (3)$$

We extract the a priori H₂CO information from the same monthly GEOS-Chem (Bey et al., 2001) climatology we use in our SAO OMI H₂CO retrieval. $w(z)$ are precomputed using VLIDORT (Spurr, 2006) and saved in look-up tables. These tables consider the $w(z)$ dependency with viewing geometry (SZA, VZA, and RAA), surface altitude, surface reflectance, and cloud properties. Information about the pixel surface reflectance is obtained from the Total Ozone Mapping Instrument (TOMS) climatology (Changwoo Ahn, personal communication, 2015). This surface reflectance climatology is the same one that is used by Vasilkov et al. (2014) to retrieve cloud information (Φ and c_{p}). Given the small variation of the AMF within the fitting interval (usually less than 7 %), we calculate it at one wavelength (λ), 340 nm, which we consider representative of their mean value within the fitting window. A detailed description of AMF calculations can be found in González Abad et al. (2015).

2.2.3 Reference sector normalization of VCDs

We are retrieving ΔSCDs due to the fact that we are using a radiance reference as a starting point in the modeling of radiances. To obtain SCDs starting from these ΔSCDs we calculate a normalization to modeled values. We work out the difference between the retrieval over the Pacific Ocean and the GEOS-Chem climatology. The process, inspired by earlier work by Khokhar et al. (2005) and De Smedt et al. (2008), is described in detail by González Abad et al. (2015). Here we mention the essential steps and ideas behind it.

Using the same radiance reference we perform two retrievals. One retrieval is for the orbit of interest, for example a satellite flight over Africa and Europe, and the second one is the retrieval of the orbit we used to compute the radiance reference which is always over the remote Pacific Ocean. Using the second retrieval and the monthly GEOS-Chem climatology we work out a latitudinally dependent correction which accounts for the difference between the ΔSCDs and the model SCDs. This correction is different for each radiance reference, so it changes daily, and is applied only to orbits retrieved with that particular radiance reference. We then assume that this correction is longitudinally constant so that we can apply the correction to results from the orbit-of-interest retrieval. Before applying the correction we take into account the particularities of each scene by using the information contained in the AMFs. Equations (4) and (5) summarize the basic operations involved in the process.

$$\mathrm{Corr(lat)} = \mathrm{MEDIAN}\big[(\mathrm{VCD_{GEOS}} \times \mathrm{AMF}_j) - \Delta\mathrm{SCD}_j\big] \quad (4)$$

We work out the amplitude of the correction at 500 latitude grid points extending from 90° N to 90° S. To obtain the value for each grid point we consider the median value of all j pixels of the radiance reference orbit whose central latitudes are in between any given couple of contiguous grid points. After interpolating the correction to the latitude value of each pixel (i) in the orbit of interest we apply the information contained in the particular AMF to that pixel to obtain the reference sector corrected VCD.

$$\mathrm{VCD}_i = \frac{\mathrm{Corr(lat}_i) + \Delta\mathrm{SCD}_i}{\mathrm{AMF}_i} \quad (5)$$

Figure 4 shows ΔVCDs (defined as ΔSCD/AMF), VCDs, ΔVCDs fitting uncertainty and RMS for orbit 6202 a January 2013 overpass of Africa and Europe. Enhanced concentrations in the middle of the orbit correspond to hotspots over Central Africa.

3 Error analysis

For an individual pixel VCD the associated error ($\varepsilon_{\mathrm{VCD}}$) is given by Eq. (6), which assumes no correlation between terms. Given the small contributions arising from correlations, this is a good approximation for the description of the VCD error (Boersma et al., 2004).

$$\varepsilon_{\mathrm{VCD}}^2 = \frac{\varepsilon_{\Delta\mathrm{SCD_{random}}}^2}{\mathrm{AMF}^2} + \frac{\varepsilon_{\Delta\mathrm{SCD_{sys}}}^2}{\mathrm{AMF}^2} + \left(\frac{\mathrm{Corr}}{\mathrm{AMF}^2}\right)^2 \varepsilon_{\mathrm{AMF}}^2 + \frac{\varepsilon_{\mathrm{Corr}}^2}{\mathrm{AMF}^2} \quad (6)$$

In Eq. (6), $\varepsilon_{\Delta\mathrm{SCD_{ramdon}}}$ is the random component of the spectral fitting process. It can be estimated by considering the residuals of the fitting process according to Eq. (7), which takes into consideration the diagonal term of the covariance matrix for H$_2$CO (C_j) and the RMS fitting residual weighted by the degrees of freedom (m is the number of spectral points and n the number of fitted variables). This method to estimate $\varepsilon_{\Delta\mathrm{SCD_{ramdon}}}$ also includes contributions from systematic errors that consistently show up in the fitting residuals. To evaluate them we have computed an average residual ("common mode") for each cross-track position and included it in the semi-empirical calculation of the radiances (Eq. 1) as an extra term. The difference in the fitting uncertainty between retrievals performed with and without the common mode is about 25 %. We attribute this difference to systematic errors due to instrumental effects such as characterization of the instrumental line shape, wavelength calibration, and stray light. As mentioned in Sect. 2.2.1, $\varepsilon_{\Delta\mathrm{SCD_{ramdon}}}$ values range between 10 % over H$_2$CO hotspots to 100 % or more for pixels with low concentrations.

$$\varepsilon_{\Delta\mathrm{SCD_{random}}}^2 = \mathrm{RMS}^2 \left(\frac{m}{m-n}\right)(C_j C_j) \quad (7)$$

We have evaluated the systematic component of ΔSCD error ($\varepsilon_{\Delta\mathrm{SCD_{sys}}}$) considering only the error associated with the uncertainties of the different cross sections included in the semi-empirical model of the radiances (Eq. 1). Table 2 summarizes the uncertainties associated to each molecule as reported in the literature. Considering that the uncertainties for different cross sections are not correlated we have found $\varepsilon_{\Delta\mathrm{SCD_{sys}}}$ to be about 7 %.

To estimate the error associated with AMF calculations we have performed a sensitivity analysis by perturbing one at the time the input parameters of AMF calculations. The parameters considered are cloud parameters, surface reflectance, terrain height, and GEOS-Chem climatological profiles as well as the wavelength dependency of $w(s)$ within the fitting window. The amplitude of each perturbation is reflecting the uncertainties reported in the literature for each one of the parameters. A shortcoming of this method is that it assumes that errors due to different parameters are not correlated.

We already mentioned that the dependency with λ of $w(z)$ is weak, around 7 %; by choosing a λ near the center of the fitting window, 340 nm, we estimate that the error due to the variation of $w(z)$ in the fitting window is about 4 %. In the UV spectral range, most surfaces reflect between 1 and 10 % of the incoming light. The errors of the TOMS surface climatology are estimated to be around 40 %, which translates to an error of 6 % in the AMF for a typical surface with an albedo of 0.03. Brighter surfaces such as deserts with albedos of 0.1 will have an AMF error of 14 %, while for a snowy

Table 2. Systematic uncertainties of the cross sections included in the fitting of H$_2$CO.

| Molecule	Data source	Cross-section error %
H$_2$CO 300 K	Chance and Orphal (2011)	5 %
O$_3$ 228 K and 295 K	Malicet et al. (1995)	2 %
NO$_2$ 220 K	Vandaele et al. (1998)	3 %
BrO 228 K	Wilmouth et al. (1999)	8 %
O$_2$−O$_2$ collision complex 293 K	Thalman and Volkamer (2013)	3 %
Ring effect	Chance and Spurr (1997)	5 %
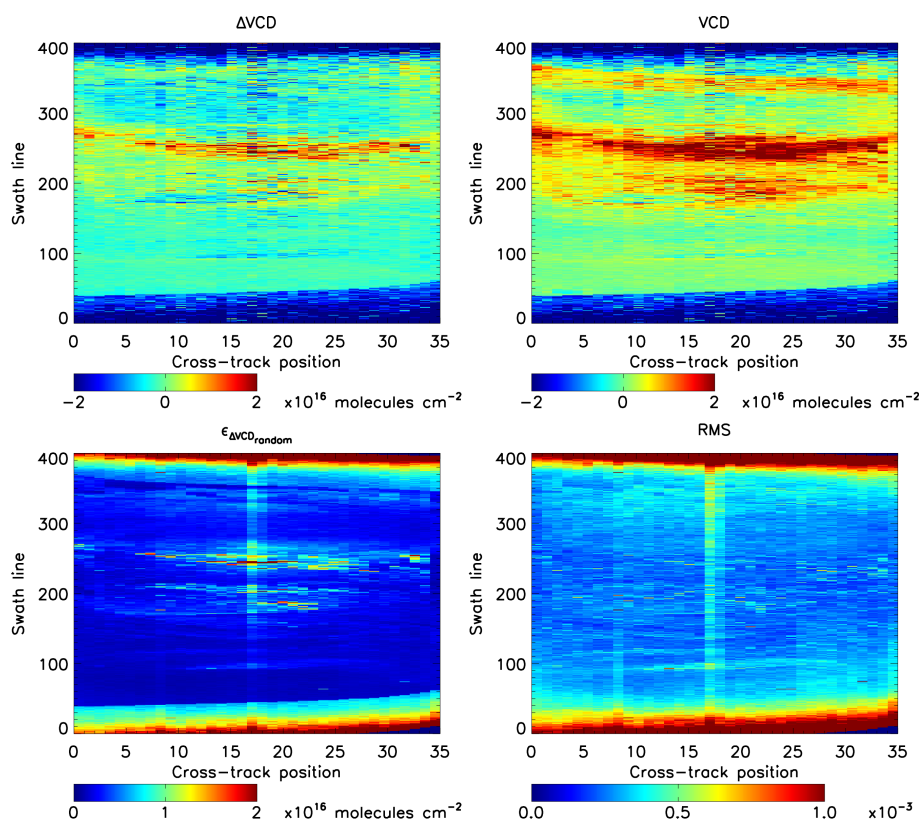
Figure 4. Africa and Europe overpass: retrieval for orbit 6202 during January 2013. VCDs corrected with the reference sector from the Ocean Pacific are depicted in top right panel while original ΔVCDs are shown in top left panel. Bottom two panels show the fitting uncertainty, which shows no effect of the SAA in contrast to those shown in Fig. 3, and RMS values, by which is possible to see the effect of splitting the central cross-track pixel in two cross-track positions (Seftor et al., 2014).

pixel with an albedo of 0.4 the AMF error will be about 26 %. A change in the cloud pressure from 800 to 900 hPa will imply a change in the AMF from 0.6 to 1.2. The cloud product we are using is derived from analysis of the rotational Raman scattering around 350 nm (Vasilkov et al., 2014). Errors of the cloud centroid pressure are estimated to be about 50 hPa, which translates to variations in the AMF values of 23 %. A change in the cloud fraction of 0.1 for a cloud pressure of 800 hPa will change the AMF by 25 %. To finish the sensitivity analysis of the AMF calculation we tested the impact of the a priori profiles of H$_2$CO. Since it is the shape of

the profile what affects the AMF calculation we have applied the reported uncertainty only to layers showing the highest volume mixing ratios, defined as those that contribute to the 90 % percentile concentrations. Those uncertainties are defined as the GEOS-Chem biases with respect to in situ measurements. GEOS-Chem biases vary with location around the world. For example, GEOS-Chem simulations over the USA have biases of around 10 % (Millet et al., 2006), which translate to AMF uncertainties up to 16 %, while over tropical regions Barkley et al. (2011) reported biases up to 25 %, which translate to 40 % AMFs uncertainties.
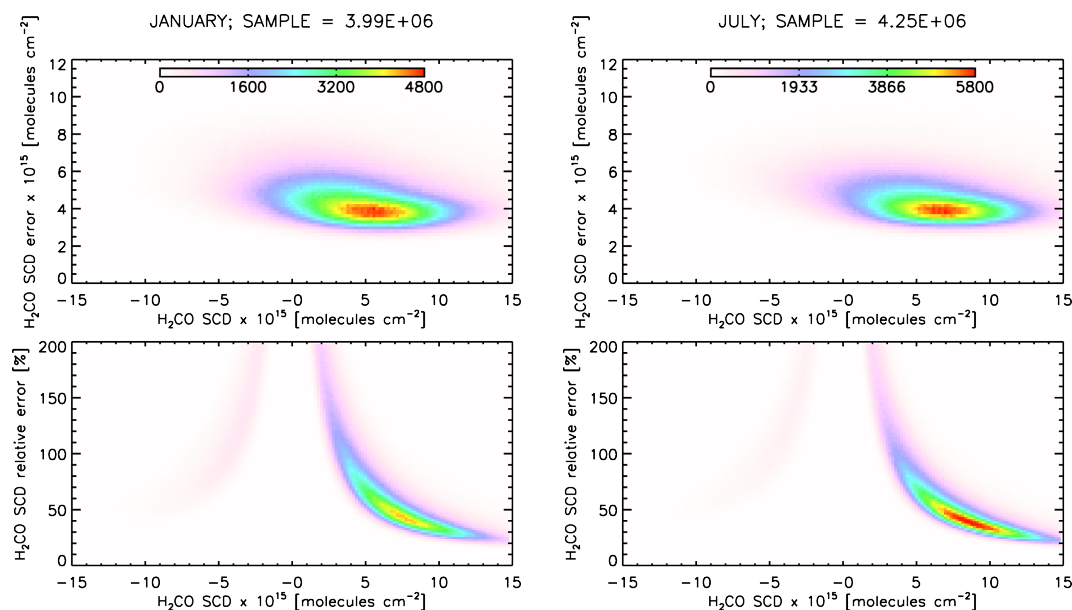
Figure 5. Absolute (top panels) and relative (bottom panels) error density probability functions vs. retrieved slant column for January (left panels) and July (right panels). Only pixels with SZA smaller than 70° have been considered in the calculation of the DPFs.
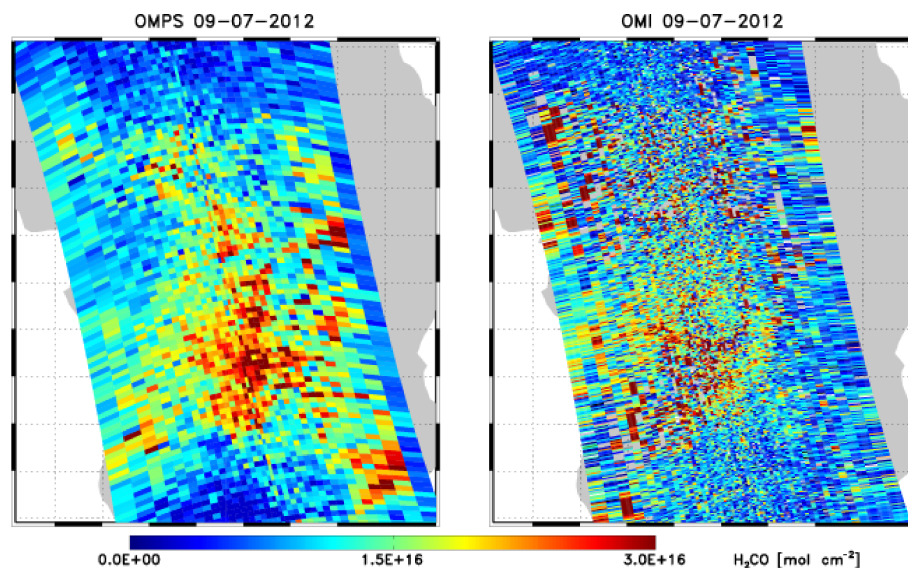
Figure 6. Africa overpass H₂CO retrieval on 9 September 2012 for OMPS (left panel) and OMI (right panel) illustrating the difference in pixel size between both instruments. Since 2008 OMI orbits have been affected by the row anomaly. We have not filtered out OMI pixels affected by it.

Considering the contributions from all these factors we estimate $\varepsilon_{\mathrm{AMF}}$ to be about 38 %, for an optimistic case with small GEOS-Chem profile uncertainty and cloud parameters being the most significant source of uncertainty, to 50 % when surface reflectance and GEOS-Chem profile uncertainties are at their maximum, becoming significant sources of AMF uncertainty that contribute as much as the uncertainty in the cloud parameters.

Finally we consider $\varepsilon_{\mathrm{Corr}}$, the error associated with the GEOS-Chem climatology used to perform the reference sector correction. As mentioned above this climatology is estimated to have a 10 % error, which we have assumed to be directly carried over to the final H₂CO VCDs. This assumption intentionally provides a high error estimate.

To summarize, users of this product should assume that a typical pixel VCD will have an uncertainty ranging between 40 and 100 % for hotspots and background level concentra-

tion pixels, respectively. This conclusion can be appreciated better in Fig. 5. Here we show absolute and relative error density probability functions (DPFs) for all orbits available in the months of January and July. Four million pixels are used in the calculation of January's DPFs while 4 million and a quarter are used for July's DPFs. The first conclusion is that the shape of the distribution is similar for both months but there are some differences. The relative error DPF peaks at 38 % in January and 36 % in July and both have a minimum relative error cutoff around 15 %. January errors are more spread than July errors. For example, in January 46 % of the pixels have relative errors below 60 and 73 % errors below 100 %, while in July these numbers increase to 54 and 79 %. This behavior is not surprising when we consider the higher concentrations observed in July vs. the concentrations observed in January: 58 % of the pixels in January have retrieved concentrations above 5×10^{15} molecules cm^{-2} while in July this percentage increases to 68 %.

4 Comparison between OMI and OMPS H$_2$CO retrievals

We have compared our retrieval with two OMI retrievals using monthly mean averaged VCDs at a spatial resolution of $0.25° \times 0.25°$ for the time period of August 2012 to August 2013. We have only considered pixels with SZA smaller than 70° and radiative cloud fraction below 40 %. We have explored the impact of using other radiative cloud fraction to filter pixels with results from the OMPS and OMI SAO retrievals. The results for different cloud fractions are consistent between them with the exception of winter months in southeastern USA and Europe. This situation is most likely due to the reduced total columns for those months, the viewing conditions with higher SZAs, and the reduced planetary boundary layer. One question that remains to be answered for future studies combining both OMI and OMPS products is which radiative fractions threshold should be used with each product to best combine them.

OMI pixels affected by the row anomaly were discarded. The OMI retrievals used for this comparison exercise are the BIRA retrieval (De Smedt et al., 2015) v14 downloaded from the TEMIS web page (http://h2co.aeronomie.be/, De Smedt et al., 2015) and the SAO OMI retrieval v3.0.2 (González Abad et al., 2015) available from NASA's web page (http://disc.sci.gsfc.nasa.gov/Aura/data-holdings/OMI/omhcho_v003.shtml).

Two of the most significant advantages of comparing OMPS with OMI are the close overpass time for both instruments, around 13:30 LT, and the similar concepts of the instruments. Both designs use 2-D CCD detectors. A significant disadvantage is their difference in the spatial pixel size. Figure 6 shows an almost coincident OMPS and OMI Africa overpass to better illustrate the differences in the pixel size. OMI has a nadir pixel size of 24×13 km while OMPS,

**Table 3.** Geographical limits of the regions depicted in Fig. 6.

Region	Geographical limits
Pacific Ocean	30° S to 30° N
	165 to 175° W
Southeastern USA	30 to 41° N
	77 to 95° W
Amazon basin	15° S to 0°
	50 to 70° W
Europe	40 to 52° N
	0° to 25° E
Southeastern Asia	5° S to 5° N
	95 to 120° E
Tropical Africa	1.5° S to 11° N
	8° W to 30° E
Southern Africa	25 to 10° S
	17 to 33° E
East China	28 to 39° N
	111 to 120° E

Table 4. Linear Pearson coefficient of the temporal correlation between monthly mean time series shown in Fig. 8.

Region	OMI BIRA vs. OMPS	OMI SAO vs. OMPS	OMI BIRA vs. OMI SAO
Pacific Ocean	0.25	0.72	0.33
Southeastern USA	0.90	0.99	0.93
Amazon basin	0.96	0.99	0.97
Europe	0.73	0.77	0.78
Southeastern Asia	0.79	0.86	0.89
Tropical Africa	0.88	0.97	0.91
Southern Africa	0.80	0.95	0.89
East China	0.94	0.96	0.96

in the configuration we are using, has a nadir pixel size of 50×50 km. The apparent reduction of noise in OMPS retrievals in comparison with the OMI retrievals shown in Fig. 6 is a direct consequence of OMPS lower spatial and spectral resolution, which translate to signal-to-noise ratio (SNR) increases.

Figure 7 shows the eight regions we have selected for comparison. The limits are explicitly shown in Table 3. The three retrievals are able to capture the seasonality of H$_2$CO columns, showing similar patterns, as seen in Fig. 8 where we have plotted the time series of monthly means for the different regions. The error bars are the standard deviations of the pixels included in the calculation of monthly means. Temporal correlations between OMI BIRA and OMPS SAO retrievals (see Table 4 for more details) vary between a low of 0.25 over the Pacific Ocean and a maximum of 0.96 over the Amazon basin. When comparing OMI SAO and OMPS retrievals these correlations improve with a minimum of 0.72 over the Pacific Ocean and a maximum of 0.99 over the Amazon basin.
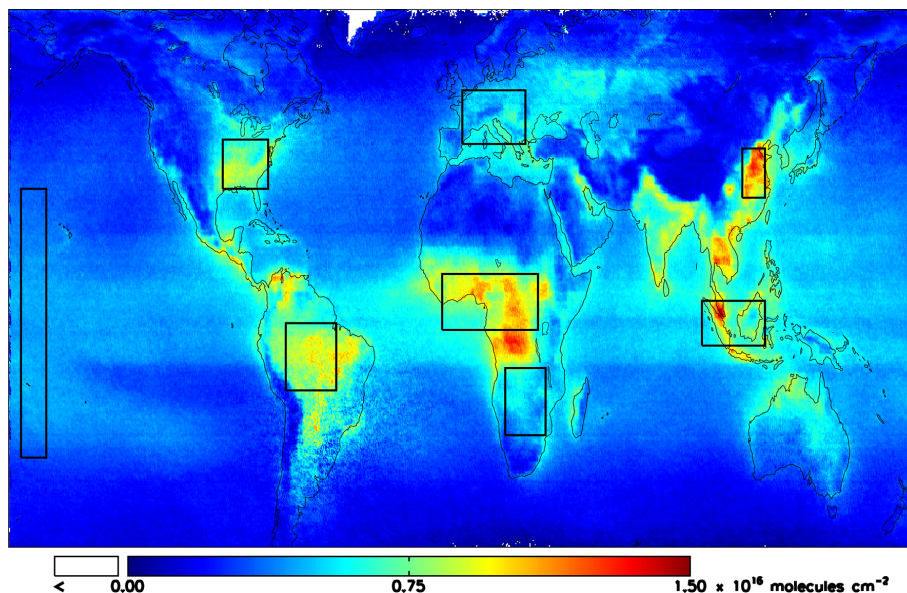
Figure 7. OMPS SAO H$_2$CO (January through September 2013) global mean at a resolution of $0.25° \times 0.25°$ showing the eight regions used in the comparison of OMPS SAO, OMI BIRA, and OMI SAO retrievals. Seven of these regions have enhanced H$_2$CO concentrations linked to biogenic, anthropogenic, and biomass burning processes. The eighth region, the Pacific Ocean, shows background concentrations of H$_2$CO due to CH$_4$ oxidation.
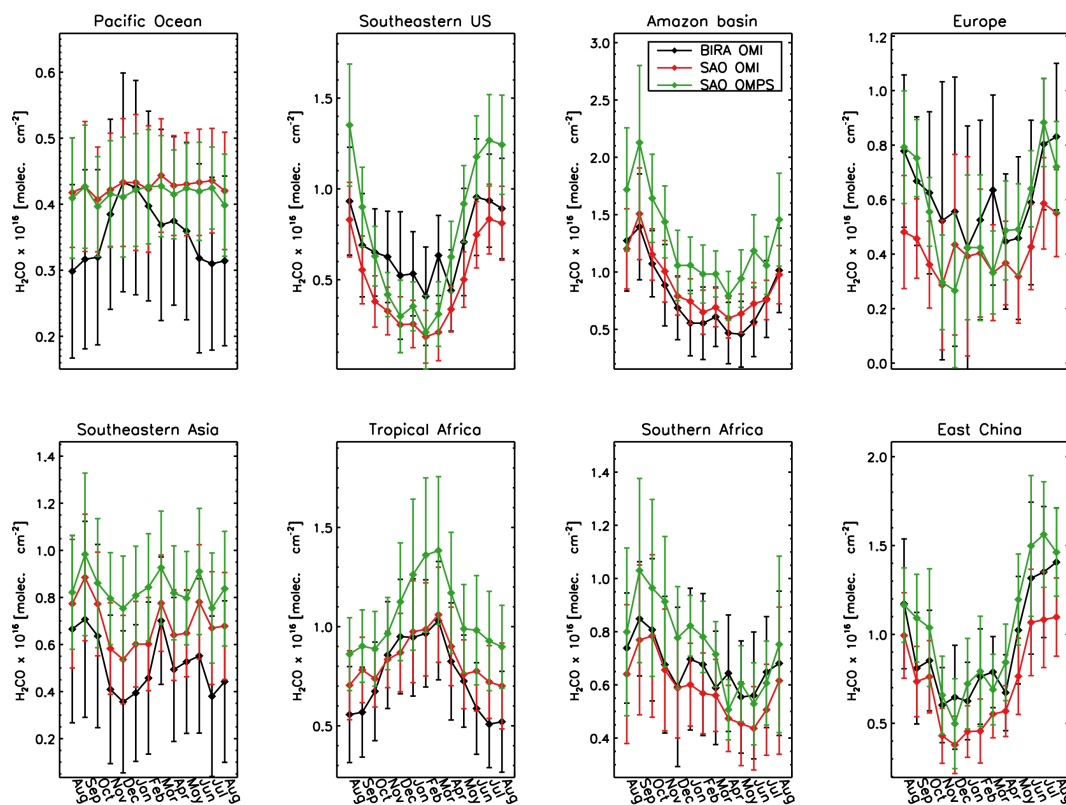
Figure 8. Monthly means between August 2012 and August 2013 for the eight regions depicted in Fig. 6. Error bars represent the standard deviation of the mean value with in the region. Green lines and data points represent OMPS SAO retrievals, red is used for OMI SAO, and black for OMI BIRA. The shapes of seasonal cycles are reproduced similarly by the three retrievals despite having significant offsets, which are further analyzed in Fig. 8.

The three retrievals, however, observe different amplitudes of seasonal variations. There is also a bias that can be significant for particular months and regions. The difference between the BIRA and SAO retrievals over the Pacific Ocean is induced by the underlying difference of the chemical transport models used for the reference sector correction. As expected, the differences between OMI BIRA and OMPS retrievals are greater than those between OMI SAO and OMPS. The absolute mean offset between the OMPS SAO retrieval and the OMI BIRA is 28 %, while it is 23 % between OMI SAO and OMPS. Part of the bias between both SAO products can be explained by the differences in the AMFs. Despite using the same scattering weight look-up tables, as well as GEOS-Chem climatology, the differences between OMI and OMPS cloud products as well as surface reflectance are the cause for OMI SAO AMFs to be on average 10 % higher than OMPS SAO AMFs. This difference in AMFs can explain 10 % of the quasi-systematic 23 % low bias of OMI SAO with respect to OMPS SAO retrievals.

While these mean absolute offsets give us an idea of how close the retrievals are, from a general perspective it is more interesting to consider the differences for particular regions. The most evident differences between OMI BIRA and OMPS, easy to appreciate in Fig. 9, happen during the winter months over southeastern USA and Europe. For example, in December over southeastern USA the bias between OMI BIRA and OMPS is 75 % while between OMI SAO and OMPS is −16 %. During the same month over Europe the differences are 109 % between OMI BIRA and OMPS and 63 % between OMI SAO and OMPS. Table 5 summarizes the amplitude, maximum, and minimum of the yearly variation for each one of the retrievals and regions. The amplitude observed with OMPS is in general bigger than the amplitude observed with OMI; however, considering the errors associated with each derived amplitude the values obtained with all three retrievals for each region always fall within the error bars. We would like to remind any possible user of these products of the increased difficulty of winter retrievals over Europe due to the viewing geometry (high SZA).

With few exceptions (winter months over southeastern USA, Europe, and eastern China) retrieved H$_2$CO VCDs using OMPS are higher than columns retrieved using OMI as shown by the dominant blue color in Fig. 9. This figure shows the bias between OMPS and OMI retrievals as the percentage of OMI minus OMPS over OMPS. It is clear that to have a better idea of the accuracy of the different retrievals, independent validation studies like the one recently published by Zhu et al. (2016) are needed. In this paper H$_2$CO satellite products produced from different groups using different instruments are compared with in situ measurements. The products included in this comparison are BIRA OMI, GOME2A and GOME2B, SAO OMI and OMPS, and NASA Goddard OMPS. SAO OMPS retrievals are found to be biased 39 % lower over the southeastern USA between 5 August and 25 September 2013.

The error bars of Fig. 8 contain information about the variation within each region and month expressed as the standard deviation of the VCDs considered for each monthly mean calculation. In general we observe a stronger variability within one region and one month in the BIRA retrieval than in the SAO retrievals. The average VCDs variability for the retrievals considering all regions and months is 2.6×10^{15} molecules cm^{-2} for OMI BIRA, 1.9×10^{15} molecules cm^{-2} for OMI SAO, and 2.2×10^{15} molecules cm^{-2} for the OMPS SAO retrieval. We have included Fig. 10 showing the standard deviation for each retrieval, month, and region.

5 Conclusions

We have developed a new OMPS H$_2$CO retrieval by adapting the OMI SAO H$_2$CO retrieval to OMPS-NM. Our two-step retrieval includes the direct fitting of radiances to obtain ΔSCDs, the calculation of AMFs to convert ΔSCDs to ΔVCDs, and the application of a reference sector correction based on a monthly climatology derived from GEOS-Chem simulations to obtain the final VCDs. Despite the reduced spectral resolution of OMPS (1 nm) with respect to other sensors like OMI or GOME-2, the retrievals presented here provide compelling evidence of the suitability of OMPS-NM sensor to perform H$_2$CO retrievals. Even more, given the good SNR of OMPS-NM the retrieval has reduced noise compared with OMI retrievals and a detection limit of 7.5×10^{15} vs. 1×10^{16} molecules cm^{-2} in the case of the OMI SAO retrieval. The improved SNR (and detection limit) comes in part from the bigger number of photons captured by larger spatial pixels by OMPS-NM with respect to OMI pixels as well as the reduced OMPS spectral resolution. Typical values of the OMPS H$_2$CO VCDs range between 0.5×10^{16} and 2×10^{16} molecules cm^{-2} with associated errors of around 40 % over pixels with high concentrations that increase to 100 % or even more for pixels with low concentrations.

We have compared the OMPS SAO retrieval with OMI retrievals developed at BIRA and SAO. While all three retrievals similarly capture the general trends of seasonal variation, they show significant differences in the amplitude of the seasonal signals with significant offsets between them as well. As expected, the agreement between the SAO retrievals is better than the agreement between the SAO OMPS and BIRA OMI retrieval. The mean offset for selected regions with strong seasonal variations plus the remote Pacific Ocean is 23 % between the SAO retrievals and 28 % between the SAO OMPS and OMI BIRA retrievals. Obviously, to have an assessment of the absolute accuracy of the retrieval it is necessary to perform validation studies with independent in situ data. These studies are outside of the scope of this paper but will constitute part of ongoing efforts to validate the latest version of the SAO OMI retrieval.

Table 5. Minimum (Min.), maximum (Max.), and amplitude (Amp.) of monthly mean time series for each region and retrieval. H$_2$CO VCDs are expressed in 10^{15} molecules cm^{-2}. The error associated with each value is the standard deviation of the values considered in the calculation of the monthly mean. In parentheses, the month in which the minimum or the maximum was observed is indicated.
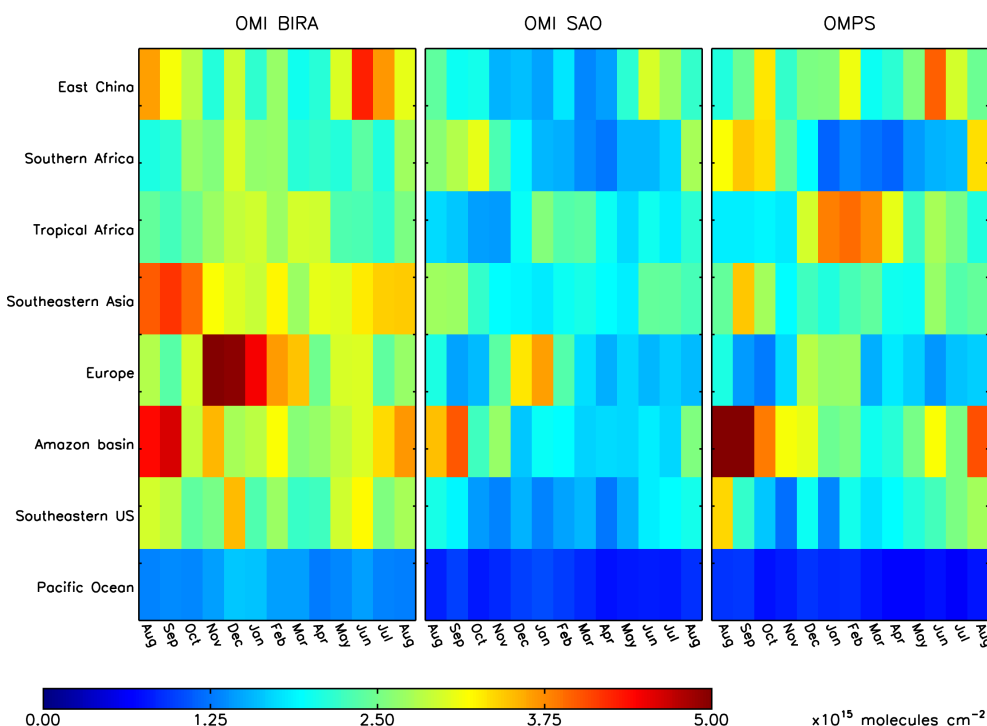
Region	OMI BIRA			OMI SAO			OMPS		
	Min.	Max.	Amp.	Min.	Max.	Amp.	Min.	Max.	Amp.
Pacific Ocean	0.3 ± 0.1 (Aug)	0.4 ± 0.2 (Dec)	0.2 ± 0.2	0.4 ± 0.1 (Oct)	0.4 ± 0.1 (Mar)	0.0 ± 0.1	0.4 ± 0.1 (Oct)	0.4 ± 0.1 (Mar)	0.0 ± 0.1
Southeastern USA	0.4 ± 0.3 (Feb)	1.0 ± 0.3 (Jul)	0.6 ± 0.4	0.2 ± 0.2 (Feb)	0.8 ± 0.2 (Jul)	0.6 ± 0.2	0.2 ± 0.2 (Feb)	1.3 ± 0.3 (Aug)	1.1 ± 0.4
Amazon basin	0.5 ± 0.3 (May)	1.4 ± 0.5 (Sep)	0.9 ± 0.5	0.6 ± 0.2 (Apr)	1.5 ± 0.4 (Sep)	0.9 ± 0.4	0.8 ± 0.2 (Apr)	2.1 ± 0.7 (Sep)	1.3 ± 0.7
Europe	0.4 ± 0.5 (Jan)	0.8 ± 0.3 (Aug)	0.4 ± 0.5	0.3 ± 0.2 (Nov)	0.6 ± 0.2 (Jul)	0.3 ± 0.3	0.8 ± 0.2 (Dec)	1.0 ± 0.4 (Jul)	0.2 ± 0.4
Southeastern Asia	0.4 ± 0.3 (Dec)	0.7 ± 0.4 (Sep)	0.3 ± 0.5	0.5 ± 0.2 (Dec)	0.9 ± 0.3 (Sep)	0.4 ± 0.3	0.8 ± 0.2 (Dec)	1.0 ± 0.4 (Sep)	0.2 ± 0.4
Tropical Africa	0.5 ± 0.2 (Jul)	1.0 ± 0.3 (Mar)	0.5 ± 0.4	0.7 ± 0.2 (Aug)	1.1 ± 0.2 (Mar)	0.4 ± 0.3	0.9 ± 0.2 (Aug)	1.4 ± 0.4 (Mar)	0.5 ± 0.4
Southern Africa	0.6 ± 0.2 (May)	0.9 ± 0.2 (Sep)	0.3 ± 0.3	0.4 ± 0.2 (Jun)	0.8 ± 0.3 (Oct)	0.4 ± 0.3	0.5 ± 0.1 (Apr)	1.0 ± 0.4 (Sep)	0.5 ± 0.4
East China	0.6 ± 0.2 (Nov)	1.4 ± 0.3 (Aug)	0.8 ± 0.4	0.4 ± 0.2 (Dec)	1.1 ± 0.2 (Aug)	0.7 ± 0.3	0.5 ± 0.3 (Dec)	1.6 ± 0.3 (Jul)	1.1 ± 0.4
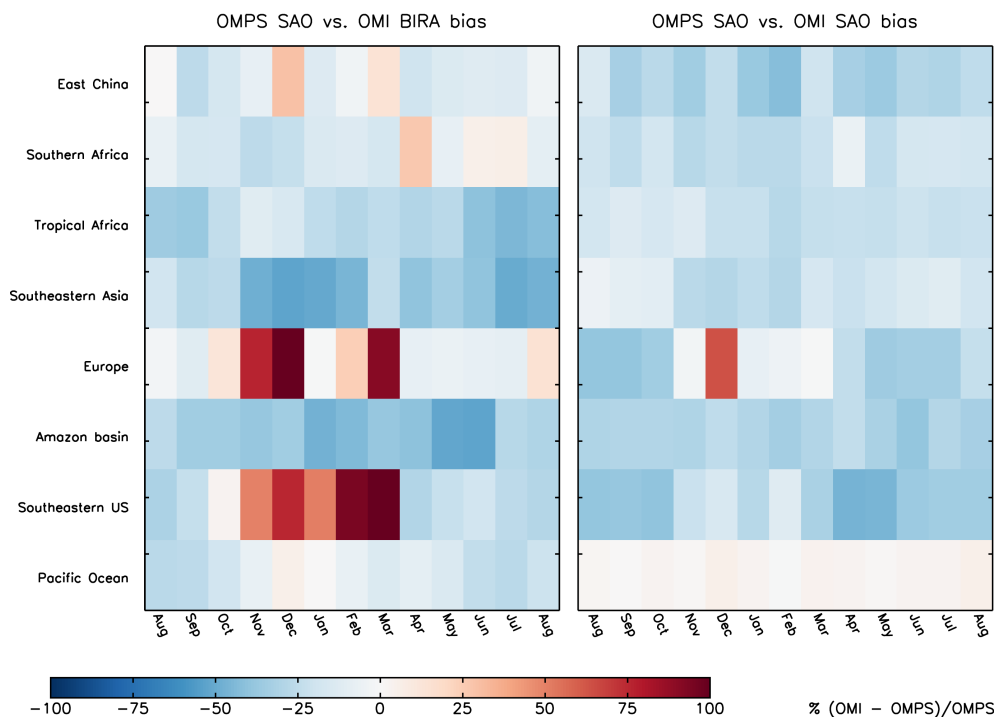
Figure 9. Monthly mean offsets between OMPS SAO retrieval and OMI retrievals from BIRA (left panel) and SAO (right panel). The offsets are expressed as percent of the OMI retrieval minus the OMPS retrieval. As expected the biases between OMPS SAO and OMI BIRA retrievals are bigger than the biases between OMPS SAO and OMI SAO. Southern Africa, Europe, and southeastern USA show the most relevant differences.

Finally we want to highlight the benefit of having similar retrievals from two instruments overlapping in time. The data record for OMI already extends for more than 10 years. OMPS was launched on board the SUOMI-NPP satellite in

October 2011 and it is therefore in the early stages of its operational life. The ongoing overlapping period between both instruments offers a great opportunity to construct a consistent extended long-term data set. To fully exploit the sci-

Figure 10. Standard deviation of the monthly means: (left panel) OMI BIRA, (middle panel) OMI SAO, and (right panel) OMPS SAO. Some regions show consistent enhanced standard deviations across retrievals for particular months, i.e., the Amazon basin between July and September and tropical Africa between December and March. These high variabilities are linked to biomass burning episodes.

entific benefits from this opportunity further studies analyzing the impact of different spectral and spatial resolutions in the retrievals of H$_2$CO are necessary. The prospect of other OMPS instruments being launched in future missions of the National Oceanic and Atmospheric Administration (NOAA) such as the Joint Polar Satellite System (JPSS) will create the possibility of a multi-decadal set of consistent measurements of H$_2$CO from afternoon LEO platforms. Another instrument that will contribute to the afternoon constellation, TROPOMI/S5P, will be launched in 2016 (Veefkind et al., 2012).

6 Data availability

SAO OMPS H$_2$CO retrievals have been performed using OMPS radiance data publicly accessible at https://ozoneaq. gsfc.nasa.gov/data/omps/ (Seftor et al., 2014). SAO OMPS H$_2$CO can be obtained by contacting the corresponding author. OMI SAO and OMI BIRA H$_2$CO retrievals are publicly available following the links included in Sect. 4.

References

Anderson, L. G., Lanning, J. A., Barrell, R., Miyagishima, J., Jones, R. H., and Wolfe, P.: Sources and sinks of formaldehyde and acetaldehyde: An analysis of Denver's ambient concentration data, Atmos. Environ., 30, 2113–2123, doi:10.1016/1352-2310(95)00175-1, 1996.

Barkley, M. P., Palmer, P. I., Kuhn, U., Kesselmeier, J., Chance, K., Kurosu, T. P., Martin, R. V., Helmig, D., and Guenther, A.: Net ecosystem fluxes of isoprene over tropical South America inferred from Global Ozone Monitoring Experiment (GOME) observations of HCHO columns, J. Geophys. Res.-Atmos., 113, D20304, doi:10.1029/2008JD009863, 2008.

Barkley, M. P., Palmer, P. I., Ganzeveld, L., Arneth, A., Hagberg, D., Karl, T., Guenther, A., Paulot, F., Wennberg, P. O., Mao, J., Kurosu, T. P., Chance, K., Müller, J.-F., De Smedt, I., Van Roozendael, M., Chen, D., Wang, Y., and Yantosca, R. M.: Can a "state of the art" chemistry transport model simulate Amazonian tropospheric chemistry?, J. Geophys. Res.-Atmos., 116, D16302, doi:10.1029/2011JD015893, 2011.

Bey, I., Jacob, D. J., Yantosca, R. M., Logan, J. A., Field, B. D., Fiore, A. M., Li, Q., Liu, H. Y., Mickley, L. J., and Schultz, M. G.: Global modeling of tropospheric chemistry with assimilated meteorology: Model description and evaluation, J. Geophys. Res.-Atmos., 106, 23073–23095, doi:10.1029/2001JD000807, 2001.

Boersma, K. F., Eskes, H. J., and Brinksma, E. J.: Error analysis for tropospheric NO_2 retrieval from space, J. Geophys. Res.-Atmos., 109, D04311, doi:10.1029/2003JD003962, 2004.

Brune, W. H., Tan, D., Faloona, I. F., Jaeglé, L., Jacob, D. J., Heikes, B. G., Snow, J., Kondo, Y., Shetter, R., Sachse, G. W., Anderson, B., Gregory, G. L., Vay, S., Singh, H. B., Davis, D. D., Crawford, J. H., and Blake, D. R.: OH and HO_2 chemistry in the North Atlantic free troposphere, Geophys. Res. Lett., 26, 3077–3080, doi:10.1029/1999GL900549, 1999.

Chance, K.: Analysis of BrO measurements from the Global Ozone Monitoring Experiment, Geophys. Res. Lett., 25, 3335–3338, doi:10.1029/98GL52359, 1998.

Chance, K. and Kurucz, R. L.: An improved high-resolution solar reference spectrum for earth's atmosphere measurements in the ultraviolet, visible, and near infrared, J. Quant. Spectrosc. Ra., 111, 1289–1295, doi:10.1016/j.jqsrt.2010.01.036, 2010.

Chance, K. and Orphal, J.: Revised ultraviolet absorption cross sections of H_2CO for the HITRAN database, J. Quant. Spectrosc. Ra., 112, 1509–1510, doi:10.1016/j.jqsrt.2011.02.002, 2011.

Chance, K., Palmer, P. I., Spurr, R. J. D., Martin, R. V., Kurosu, T. P., and Jacob, D. J.: Satellite observations of formaldehyde over North America from GOME, Geophys. Res. Lett., 27, 3461–3464, doi:10.1029/2000GL011857, 2000.

Chance, K., Kurosu, T. P., and Sioris, C. E.: Undersampling correction for array detector-based satellite spectrometers, Appl. Opt., 44, 1296–1304, doi:10.1364/AO.44.001296, 2005.

Chance, K., Liu, X., Suleiman, R. M., Flittner, D. E., Al-Saadi, J., and Janz, S. J.: Tropospheric emissions: monitoring of pollution (TEMPO), 8860, 88660D, doi:10.1117/12.2024479, 2013.

Chance, K. V. and Spurr, R. J. D.: Ring effect studies: Rayleigh scattering, including molecular parameters for rotational Raman scattering, and the Fraunhofer spectrum, Appl. Opt., 36, 5224–5230, doi:10.1364/AO.36.005224, 1997.

De Smedt, I., Müller, J.-F., Stavrakou, T., van der A, R., Eskes, H., and Van Roozendael, M.: Twelve years of global observations of formaldehyde in the troposphere using GOME and SCIAMACHY sensors, Atmos. Chem. Phys., 8, 4947–4963, doi:10.5194/acp-8-4947-2008, 2008.

De Smedt, I., Van Roozendael, M., Stavrakou, T., Müller, J.-F., Lerot, C., Theys, N., Valks, P., Hao, N., and van der A, R.: Improved retrieval of global tropospheric formaldehyde columns from GOME-2/MetOp-A addressing noise reduction and instrumental degradation issues, Atmos. Meas. Tech., 5, 2933–2949, doi:10.5194/amt-5-2933-2012, 2012.

De Smedt, I., Stavrakou, T., Hendrick, F., Danckaert, T., Vlemmix, T., Pinardi, G., Theys, N., Lerot, C., Gielen, C., Vigouroux, C., Hermans, C., Fayt, C., Veefkind, P., Müller, J.-F., and Van Roozendael, M.: Diurnal, seasonal and long-term variations of global formaldehyde columns inferred from combined OMI and GOME-2 observations, Atmos. Chem. Phys., 15, 12519–12545, doi:10.5194/acp-15-12519-2015, 2015.

Dittman, M. G., Ramberg, E., Chrisp, M., Rodriguez, J. V., Sparks, A. L., Zaun, N. H., Hendershot, P., Dixon, T., Philbrick, R. H.,

and Wasinger, D.: Nadir ultraviolet imaging spectrometer for the NPOESS Ozone Mapping and Profiler Suite(OMPS), in: Proceedings of SPIE, 4814, 111–119, 2002.

Flynn, L., Long, C., Wu, X., Evans, R., Beck, C. T., Petropavlovskikh, I., McConville, G., Yu, W., Zhang, Z., Niu, J., Beach, E., Hao, Y., Pan, C., Sen, B., Novicki, M., Zhou, S., and Seftor, C.: Performance of the Ozone Mapping and Profiler Suite (OMPS) products, J. Geophys. Res-Atmos., 119, 6181–6195, doi:10.1002/2013JD020467, 2014.

Fu, T.-M., Jacob, D. J., Palmer, P. I., Chance, K., Wang, Y. X., Barletta, B., Blake, D. R., Stanton, J. C., and Pilling, M. J.: Space-based formaldehyde measurements as constraints on volatile organic compound emissions in east and south Asia and implications for ozone, J. Geophys. Res.-Atmos., 112, D06312, doi:10.1029/2006JD007853, 2007.

González Abad, G., Liu, X., Chance, K., Wang, H., Kurosu, T. P., and Suleiman, R.: Updated Smithsonian Astrophysical Observatory Ozone Monitoring Instrument (SAO OMI) formaldehyde retrieval, Atmos. Meas. Tech., 8, 19–32, doi:10.5194/amt-8-19-2015, 2015.

Hewson, W., Barkley, M. P., Gonzalez Abad, G., Bösch, H., Kurosu, T., Spurr, R., and Tilstra, L. G.: Development and characterisation of a state-of-the-art GOME-2 formaldehyde air-mass factor algorithm, Atmos. Meas. Tech., 8, 4055–4074, doi:10.5194/amt-8-4055-2015, 2015.

Houweling, S., Dentener, F., and Lelieveld, J.: The impact of nonmethane hydrocarbon compounds on tropospheric photochemistry, J. Geophys. Res-Atmos., 103, 10673–10696, doi:10.1029/97JD03582, 1998.

Kanakidou, M., Seinfeld, J. H., Pandis, S. N., Barnes, I., Dentener, F. J., Facchini, M. C., Van Dingenen, R., Ervens, B., Nenes, A., Nielsen, C. J., Swietlicki, E., Putaud, J. P., Balkanski, Y., Fuzzi, S., Horth, J., Moortgat, G. K., Winterhalter, R., Myhre, C. E. L., Tsigaridis, K., Vignati, E., Stephanou, E. G., and Wilson, J.: Organic aerosol and global climate modelling: a review, Atmos. Chem. Phys., 5, 1053–1123, doi:10.5194/acp-5-1053-2005, 2005.

Khokhar, M., Frankenberg, C., Roozendael, M. V., Beirle, S., Kuhl, S., Richter, A., Platt, U., and Wagner, T.: Satellite observations of atmospheric SO_2 from volcanic eruptions during the time-period of 1996–2002, Adv. Space Res., 36, 879–887, doi:10.1016/j.asr.2005.04.114, 2005.

Kurosu, T. P., Chance, K., and Sioris, C. E.: Preliminary results for HCHO and BrO from the EOS-Aura Ozone Monitoring Instrument, Proc. SPIE, 5652, 116–123, doi:10.1117/12.578606, 2004.

Levelt, P. F., van den Oord, G. H. J., Dobber, M. R., Mälkki, A., Visser, H., de Vries, J., Stammes, P., Lundell, J. O. V., and Saari, H.: The ozone monitoring instrument, IEEE T. Geosci. Remote., 44, 1093–1101, doi:10.1109/TGRS.2006.872333, 2006.

Li, C., Joiner, J., Krotkov, N. A., and Dunlap, L.: A new method for global retrievals of HCHO total columns from the Suomi National Polar-orbiting Partnership Ozone Mapping and Profiler Suite, Geophys. Res. Lett., 42, 2515–2522, doi:10.1002/2015GL063204, 2015.

Lindström, P. and Wedin, P.-A.: Methods and software for nonlinear least squares problems, Technical report UMINF-133.87, Inst. of Information Processing, University of Umeå, Umeå, Sweden, 1988.

Liteplo, R. G., Beauchamp, R., Meek, M. E., and Chénier, R.: Concise International Chemical Assessment Document 40, Formaldehyde, Tech. rep., World Health Organization, http://www.who.int/ipcs/publications/cicad/en/cicad40.pdf?ua=1, 2002.

Lowe, D. C. and Schmidt, U.: Formaldehyde (HCHO) measurements in the nonurban atmosphere, J. Geosphys. Res.-Oceans, 88, 10844–10858, doi:10.1029/JC088iC15p10844, 1983.

Malicet, J., Daumont, D., Charbonnier, J., Parisse, C., Chakir, A., and Brion, J.: Ozone UV spectroscopy. II. Absorption cross-sections and temperature dependence, J. Atmos. Chem., 21, 263–273, doi:10.1007/BF00696758, 1995.

Marais, E. A., Jacob, D. J., Kurosu, T. P., Chance, K., Murphy, J. G., Reeves, C., Mills, G., Casadio, S., Millet, D. B., Barkley, M. P., Paulot, F., and Mao, J.: Isoprene emissions in Africa inferred from OMI observations of formaldehyde columns, Atmos. Chem. Phys., 12, 6219–6235, doi:10.5194/acp-12-6219-2012, 2012.

Martin, R. V., Chance, K., Jacob, D. J., Kurosu, T. P., Spurr, R. J. D., Bucsela, E., Gleason, J. F., Palmer, P. I., Bey, I., Fiore, A. M., Li, Q., Yantosca, R. M., and Koelemeijer, R. B. A.: An improved retrieval of tropospheric nitrogen dioxide from GOME, J. Geophys. Res.-Atmos., 107, ACH 9-1–ACH 9-21, doi:10.1029/2001JD001027, 2002.

Millet, D. B., Jacob, D. J., Turquety, S., Hudman, R. C., Wu, S., Fried, A., Walega, J., Heikes, B. G., Blake, D. R., Singh, H. B., Anderson, B. E., and Clarke, A. D.: Formaldehyde distribution over North America: Implications for satellite retrievals of formaldehyde columns and isoprene emission, J. Geophys. Res.-Atmos., 111, D24S02, doi:10.1029/2005JD006853, 2006.

Palmer, P. I., Jacob, D. J., Chance, K., Martin, R. V., Spurr, R. J. D., Kurosu, T. P., Bey, I., Yantosca, R., Fiore, A., and Li, Q.: Air mass factor formulation for spectroscopic measurements from satellites: Application to formaldehyde retrievals from the Global Ozone Monitoring Experiment, J. Geophys. Res-Atmos., 106, 14539–14550, doi:10.1029/2000JD900772, 2001.

Parrish, D. D., Ryerson, T. B., Mellqvist, J., Johansson, J., Fried, A., Richter, D., Walega, J. G., Washenfelder, R. A., de Gouw, J. A., Peischl, J., Aikin, K. C., McKeen, S. A., Frost, G. J., Fehsenfeld, F. C., and Herndon, S. C.: Primary and secondary sources of formaldehyde in urban atmospheres: Houston Texas region, Atmos. Chem. Phys., 12, 3273–3288, doi:10.5194/acp-12-3273-2012, 2012.

Schönhardt, A., Richter, A., Wittrock, F., Kirk, H., Oetjen, H., Roscoe, H. K., and Burrows, J. P.: Observations of iodine monoxide columns from satellite, Atmos. Chem. Phys., 8, 637–653, doi:10.5194/acp-8-637-2008, 2008.

Seftor, C. J., Jaross, G., Kowitt, M., Haken, M., Li, J., and Flynn, L. E.: Postlaunch performance of the Suomi National Polar-orbiting Partnership Ozone Mapping and Profiler Suite (OMPS) nadir sensors, J. Geophys. Res.-Atmos., 119, 4413–4428, doi:10.1002/2013JD020472, 2014.

Spurr, R. J.: VLIDORT: A linearized pseudo-spherical vector discrete ordinate radiative transfer code for forward model and retrieval studies in multilayer multiple scattering media, J. Quant. Spectrosc. Ra., 102, 316–342, doi:10.1016/j.jqsrt.2006.05.005, 2006.

Stavrakou, T., Müller, J.-F., De Smedt, I., Van Roozendael, M., van der Werf, G. R., Giglio, L., and Guenther, A.: Evaluating the performance of pyrogenic and biogenic emission inventories against one decade of space-based formaldehyde columns, Atmos. Chem. Phys., 9, 1037–1060, doi:10.5194/acp-9-1037-2009, 2009a.

Stavrakou, T., Müller, J.-F., De Smedt, I., Van Roozendael, M., van der Werf, G. R., Giglio, L., and Guenther, A.: Global emissions of non-methane hydrocarbons deduced from SCIAMACHY formaldehyde columns through 2003–2006, Atmos. Chem. Phys., 9, 3663–3679, doi:10.5194/acp-9-3663-2009, 2009b.

Stavrakou, T., Müller, J.-F., Bauwens, M., De Smedt, I., Van Roozendael, M., Guenther, A., Wild, M., and Xia, X.: Isoprene emissions over Asia 1979-2012: impact of climate and land-use changes, Atmos. Chem. Phys., 14, 4587–4605, doi:10.5194/acp-14-4587-2014, 2014.

Thalman, R. and Volkamer, R.: Temperature dependent absorption cross-sections of O$_2$-O$_2$ collision pairs between 340 and 630 nm and at atmospherically relevant pressure, Phys. Chem. Chem. Phys., 15, 15371–15381, doi:10.1039/C3CP50968K, 2013.

Vandaele, A., Hermans, C., Simon, P., Carleer, M., Colin, R., Fally, S., Mérienne, M., Jenouvrier, A., and Coquart, B.: Measurements of the NO$_2$ absorption cross-section from $42\,000\,cm^{-1}$ to $10\,000\,cm^{-1}$ (238–1000 nm) at 220 K and 294 K, J. Quant. Spectrosc. Ra., 59, 171–184, doi:10.1016/S0022-4073(97)00168-4, 1998.

Vasilkov, A., Joiner, J., and Seftor, C.: First results from a rotational Raman scattering cloud algorithm applied to the Suomi National Polar-orbiting Partnership (NPP) Ozone Mapping and Profiler Suite (OMPS) Nadir Mapper, Atmos. Meas. Tech., 7, 2897–2906, doi:10.5194/amt-7-2897-2014, 2014.

Veefkind, J. P., Aben, I., McMullan, K., Förster, H., de Vries, J., Otter, G., Claas, J., Eskes, H. J., de Haan, J. F., Kleipool, Q., van Weele, M., Hasekamp, O., Hoogeveen, R., Landgraf, J., Snel, R., Tol, P., Ingmann, P., Voors, R., Kruizinga, B., Vink, R., Visser, H., and Levelt, P. F.: TROPOMI on the ESA Sentinel-5 Precursor: A GMES mission for global observations of the atmospheric composition for climate, air quality and ozone layer applications, Remote Sens. Environ., 120, 70–83, doi:10.1016/j.rse.2011.09.027, 2012.

Veihelmann, B. and Kleipool, Q.: Reducing Along-Track Stripes in OMI-Level 2 Products, Technical report TN-OMIE-KNMI-785, KNMI, http://disc.sci.gsfc.nasa.gov/Aura/data-holdings/OMI/documents/v003/RD08_TN785_i1_Reducing_AlongTrack_Stripes.pdf, 2006.

Vrekoussis, M., Wittrock, F., Richter, A., and Burrows, J. P.: GOME-2 observations of oxygenated VOCs: what can we learn from the ratio glyoxal to formaldehyde on a global scale?, Atmos. Chem. Phys., 10, 10145–10160, doi:10.5194/acp-10-10145-2010, 2010.

Wilmouth, D. M., Hanisco, T. F., Donahue, N. M., and Anderson, J. G.: Fourier Transform Ultraviolet Spectroscopy of the A 2Π3/2 ← X 2Π3/2 Transition of BrO†, J. Phys. Chem. A, 103, 8935–8945, doi:10.1021/jp991651o, 1999.

Wittrock, F., Richter, A., Oetjen, H., Burrows, J. P., Kanakidou, M., Myriokefalitakis, S., Volkamer, R., Beirle, S., Platt, U., and Wagner, T.: Simultaneous global observations of glyoxal and formaldehyde from space, Geophys. Res. Lett., 33, L16804, doi:10.1029/2006GL026310, 2006.

Zhu, L., Jacob, D. J., Mickley, L. J., Marais, E. A., Cohan, D. S., Yoshida, Y., Duncan, B. N., González Abad, G., and Chance,

K. V.: Anthropogenic emissions of highly reactive volatile organic compounds in eastern Texas inferred from oversampling of satellite (OMI) measurements of HCHO columns, Environ. Res. Lett., 9, 114004, doi:10.1088/1748-9326/9/11/114004, 2014.

Zhu, L., Jacob, D. J., Kim, P. S., Fisher, J. A., Yu, K., Travis, K. R., Mickley, L. J., Yantosca, R. M., Sulprizio, M. P., De Smedt, I., Gonzalez Abad, G., Chance, K., Li, C., Ferrare, R., Fried, A., Hair, J. W., Hanisco, T. F., Richter, D., Scarino, A. J., Walega, J., Weibring, P., and Wolfe, G. M.: Observing atmospheric formaldehyde (HCHO) from space: validation and intercomparison of six retrievals from four satellites (OMI, GOME2A, GOME2B, OMPS) with SEAC4RS aircraft observations over the Southeast US, Atmos. Chem. Phys. Discuss., doi:10.5194/acp-2016-162, in review, 2016.